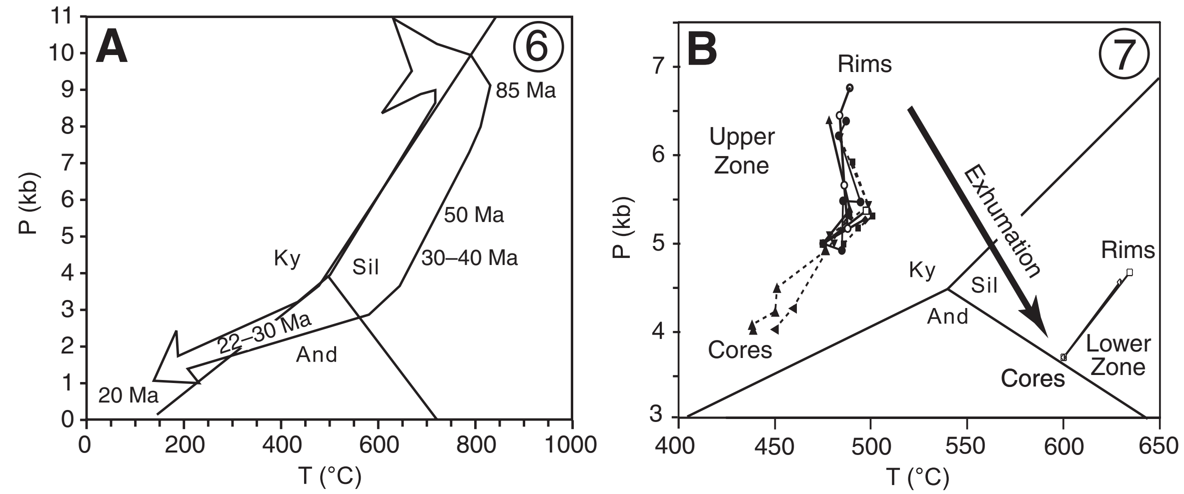


**Figure 4. P-T paths from Great Basin core complexes. (A) P-T-t path envelope determined from an array of individual P-T determinations from metabasite and metapelite of the East Humboldt Range, from McGrew et al. (2000). Interpreted decompression is corroborated by decompressional metamorphic reaction textures. (B) P-T paths from schist of Stevens Spring from the northern Grouse Creek Mountains, northwestern Utah (location R, Fig. 1). Paths from Hoisch et al. (2002) are shown as solid lines, and paths from Harris et al. (2007) are shown as dashed lines. Samples came from two zones within the schist of Stevens Spring, upper and lower, as shown, corresponding to different garnet growth reactions. $Al_2SiO_5$ polymorphic transformations are shown in solid lines (Pattison, 1992); Ky—kyanite; Sil—sillimanite; And—andalusite. Paths were determined from simulations of garnet growth zoning, using the Gibbs method on the basis of Duhem's theorem (e.g., Spear et al., 1991). Numbers in the upper right corners of both panels refer to location numbers shown in Figure 1.**

WELLS & HOISCH, GSA BULL
2008

Reminder of some of the later stage exhumation of rocks—these are found in ranges termed core complexes

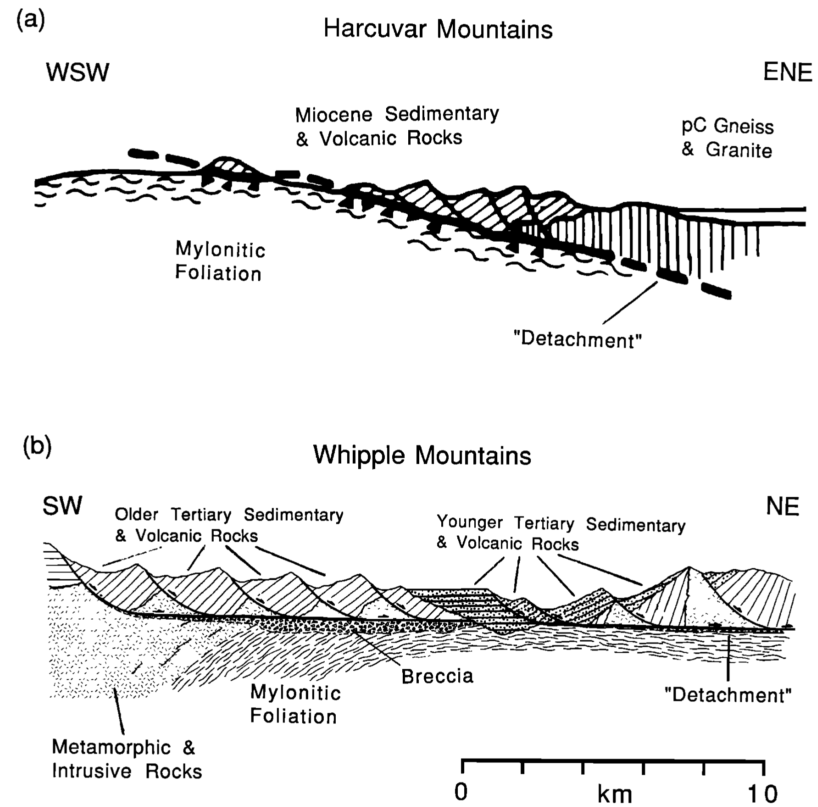


Fig. 1. Interpretative cross sections of two metamorphic core complexes showing features common to many core complexes: (a) the Harcuvar Mountains in Arizona [after Rehrig and Reynolds, 1980] and (b) the Whipple Mountains in California with inferred doming removed [after Davis, 1980].

Buck, Tectonics, 1988

# Generic core complex

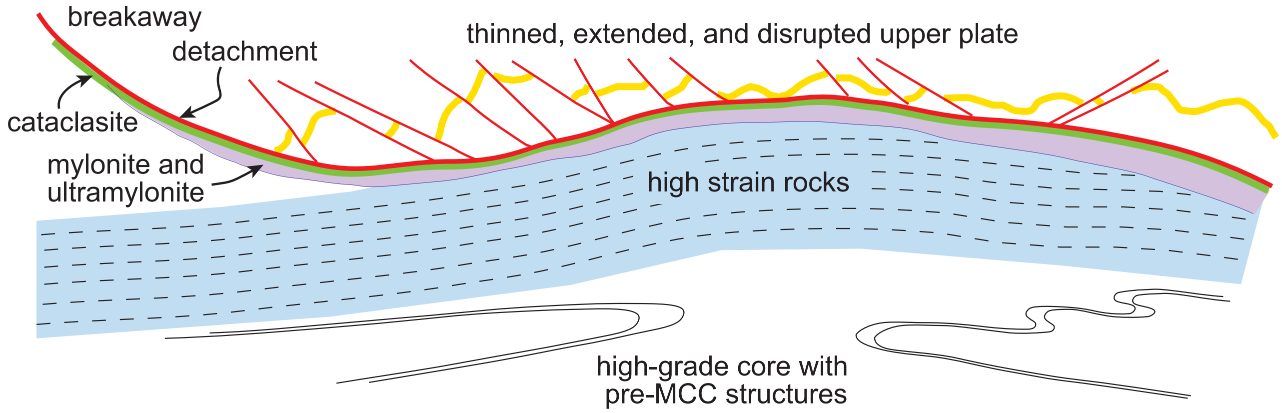


Platt, *J. Geol. Soc.*, 2015

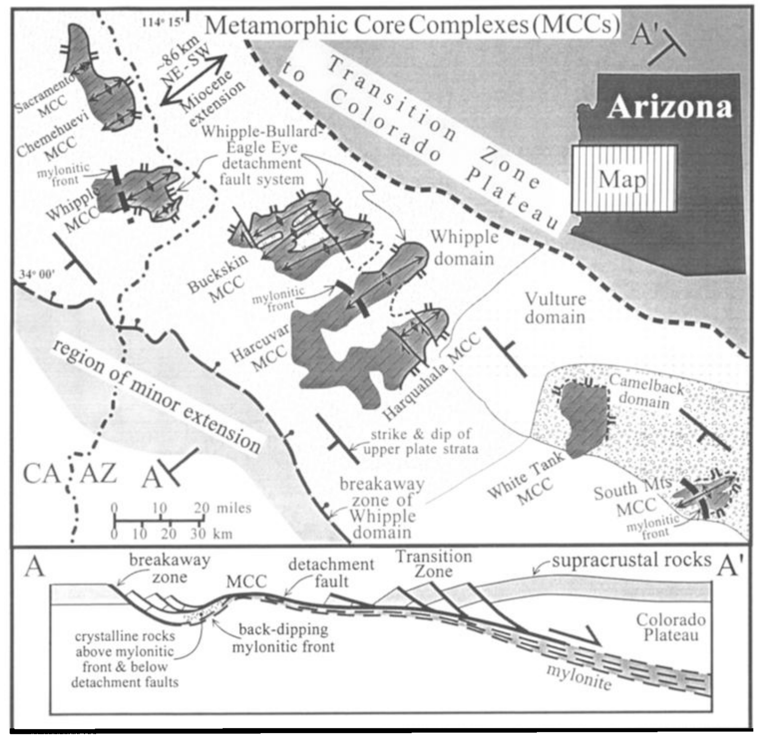


**Figure 1.** Location map, generalized geologic map and cross section (A - A') of metamorphic core complexes (MCCs) of west central Arizona and southeastern California [after *Reynolds et al.*, 1988]. The Harquahala, Harcuvar, Buckskin, Whipple, Chemehuevi, Sacramento, White Tank, and South Mountains MCCs represent antiformal arches of mylonitized footwall rocks. Normal-slip, low-angle (dip of 10° - 25°) detachment faults separate MCC footwall rocks from tilted, hanging wall strata. The Camelback, Vulture, and Whipple domains represent areas of similar regional dip of hanging wall strata [*Reynolds et a*l., 1988]. MCC footwalls and titled hanging wall strata form a zone of large-magnitude Miocene extension separating regions that experienced little Miocene extension. These little extended regions include the "Transition Zone to the Colorado Plateau" and the "region of only minor extension" southwest of the Whipple domain breakaway zone.

Livaccari and Geissman, Tectonics, 2001

These structures also vary in map view, making doubly-plunging antiforms. Look at one of these (Buckskin) in more detail

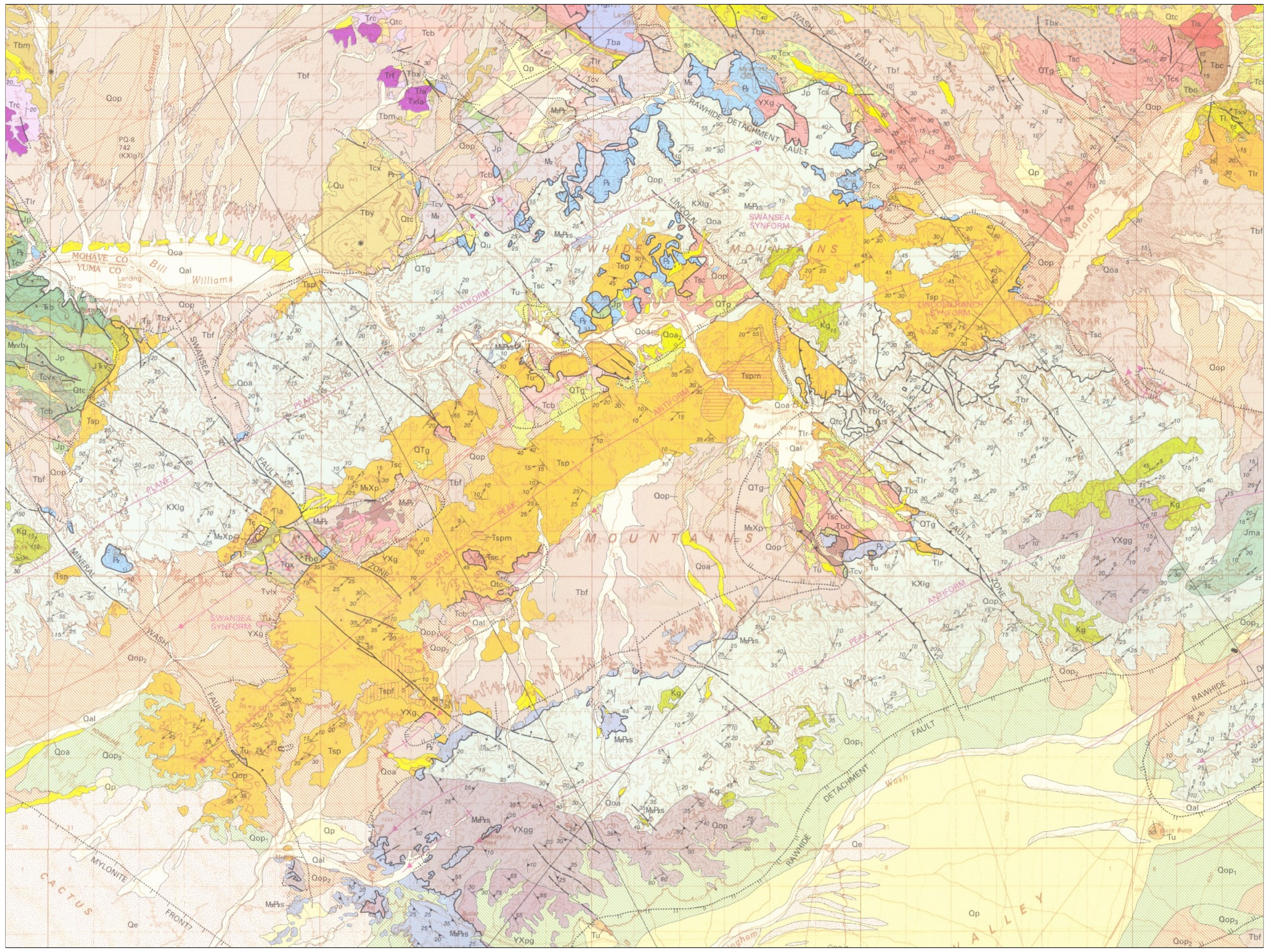

Blue in upper right upper plate.  Orange is lower plate T pluton, purple at bottom lower plate pC.

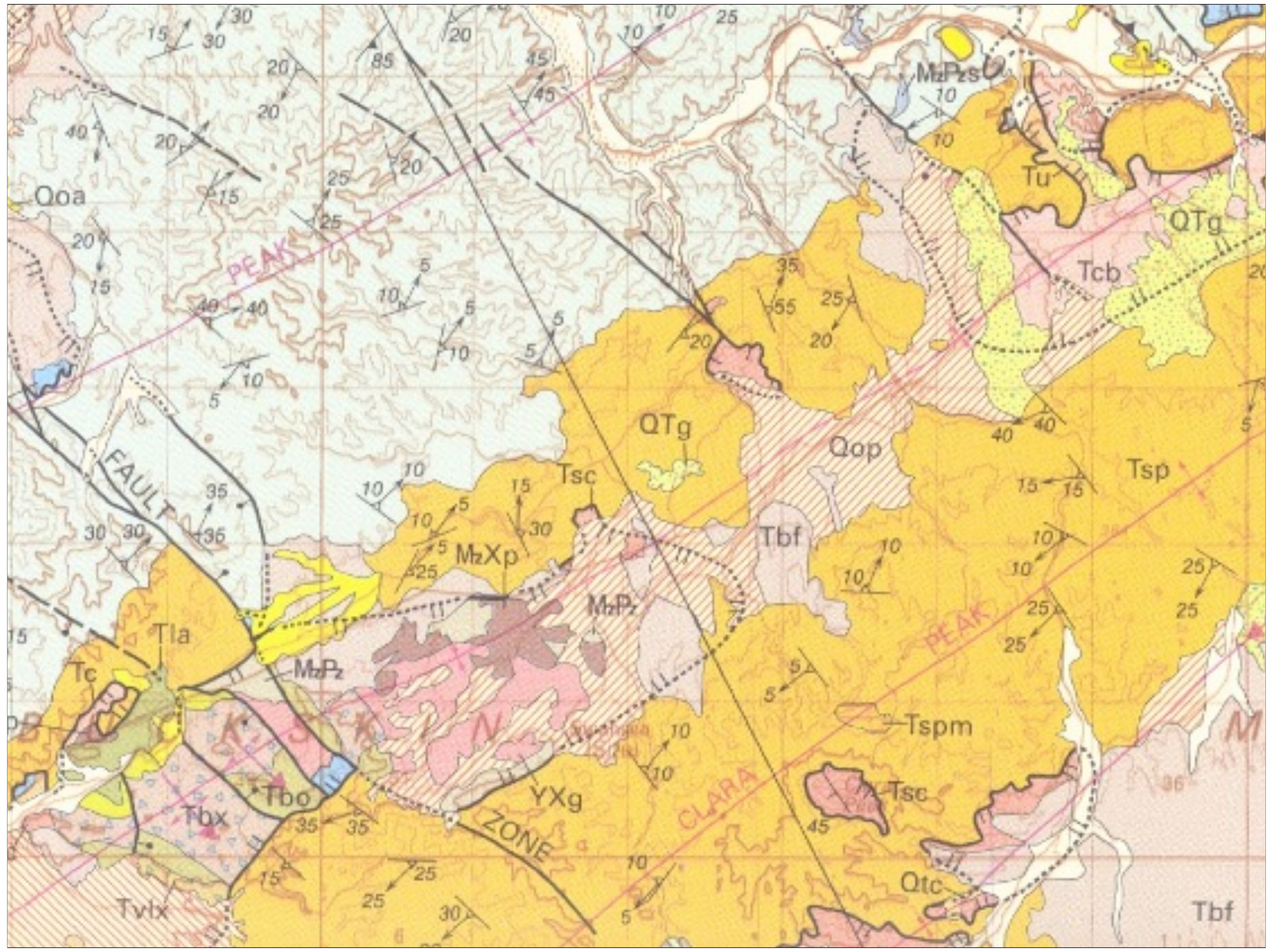

Qoa
PEAK
FAULT
ZONE
CLARA
PEAK
QTg
Tsc
M₂Xp
M₂Pz
Tla
Tc
Tbx
Tbo
Tvlx
YXg
Qop
Tbf
Tsp
Tspm
Qtc
Tu
Tcb
M₂Pzs

Rawhide Mtns from Swansea site

Red vs green, Buckskin CC

Looking into the fault

Mylonite, Buckskin Mtns

Catalina Mtns, So. AZ

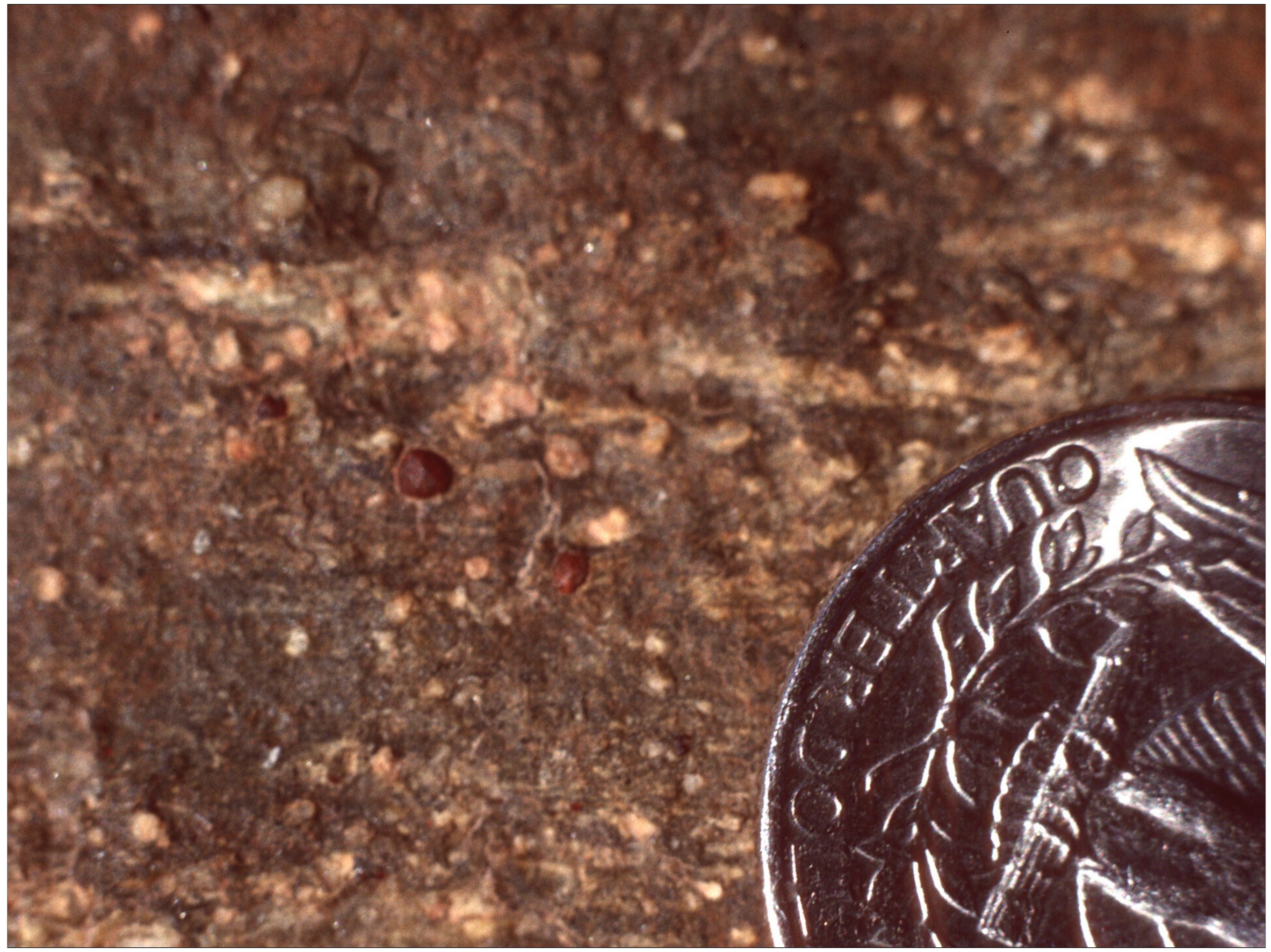

Cataclasite?


Ultramylonite, Catalina core complex (Rincon Mtns)

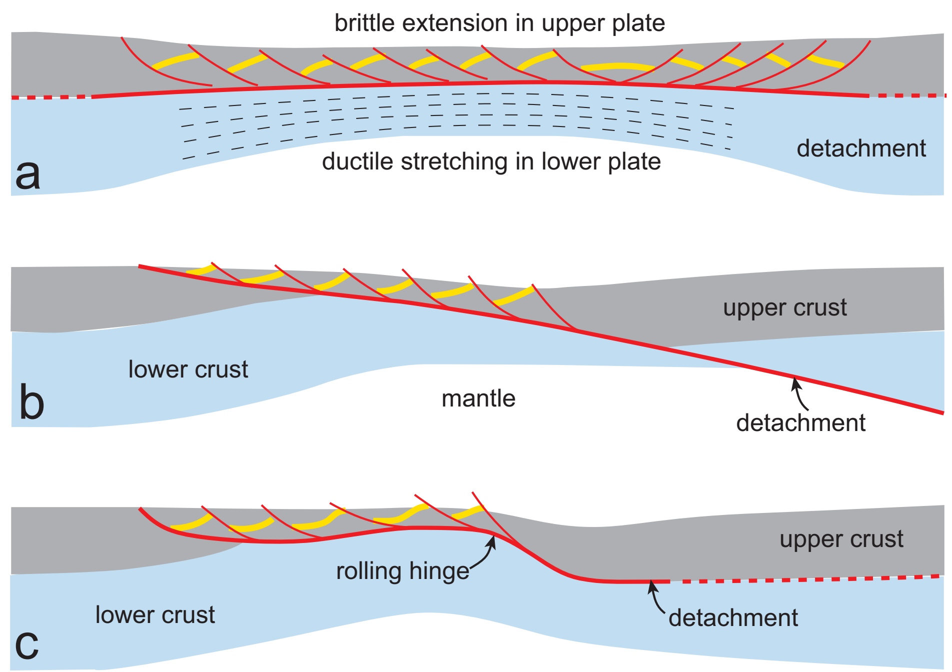


Platt, *J. Geol. Soc.*, 2015

So how are these things created?  Simple cartoons of some ideas.  Look at what the observations were that led to these.

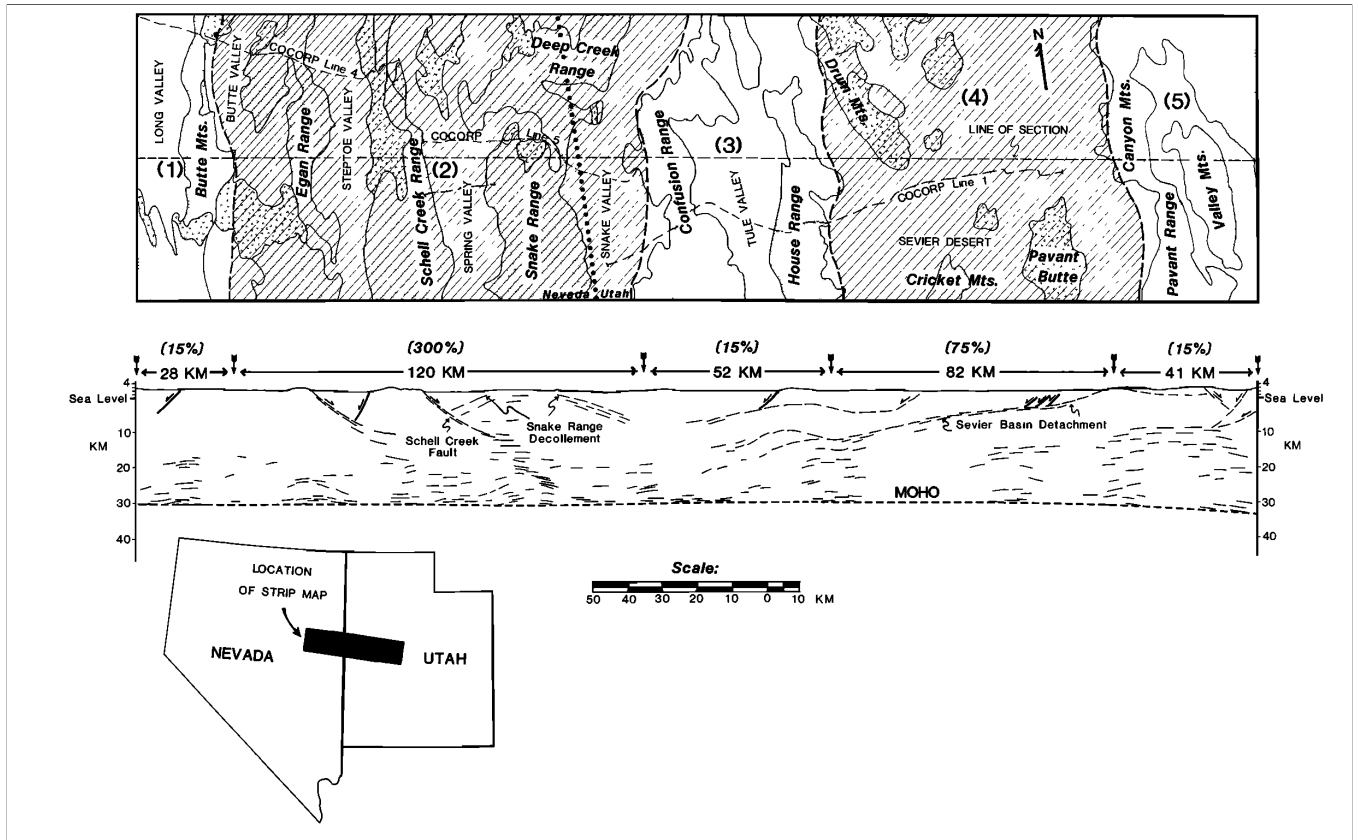


Fig. 1. Geologic strip map and generalized crustal cross section across the eastern Great Basin. Geologic map modified from Stewart and Carlson [1978] and Hintze [1980] Stippled areas represent Precambrian to Mesozoic carbonate and clastic rocks, and v represent Tertiary and Quaternary volcanic rocks. Numbered areas correspond to domain discussed in text, with the more highly extended domains highlighted with slanted lines. Subsurface information shown on the cross section is drawn largely from the seism reflection profiles described by Allmendinger et al. [1983], Hauser et al. [1984], Gans et al. [1985], McCarthy [1986], and Klemperer et al. [1986]. Depth to the reflection M was calculated assuming an average crustal velocity of 6.5 km/s.

Gans, Tectonics, 1987

First up, recognition of very variable amounts of extension but flat Moho.

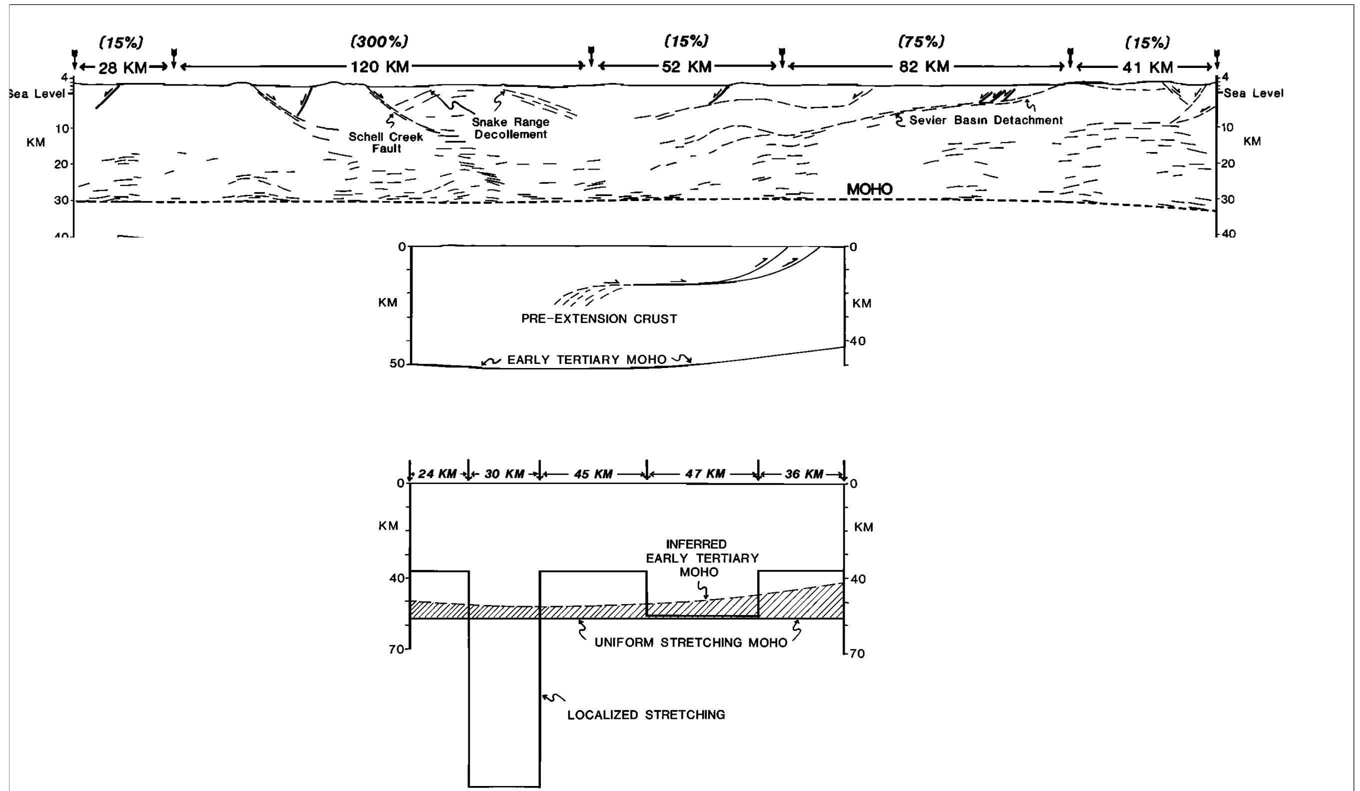


Fig. 2. (A) The inferred crustal thickness profile of the eastern Great Basin prior to the onset of extensional tectonism, as deduced from regional geological considerations and a comparison with the Canadian Cordillera. Note that the E-W dimension corresponds to the width of the transect discussed in the text after the effects of Cenozoic extension are removed. (B) The predicted preextensional Moho of the eastern Great Basin calculated using two different models for crustal stretching, neither of which incorporates additions of new material to the crust. The Localized Stretching Moho assumes pure shear of the crustal column beneath each domain by an amount equivalent to the percent extension measured at the surface. The Uniform Stretching Moho assumes pure shear of the eastern Great Basin by the average amount of extension measured across the entire transect. The hatchured area represents the amount of new material that is inferred to have been added to the crust during Tertiary stretching. See text for discussion.

Gans, Tectonics, 1987

You push things back assuming vertically uniform deformation and you get craziness.

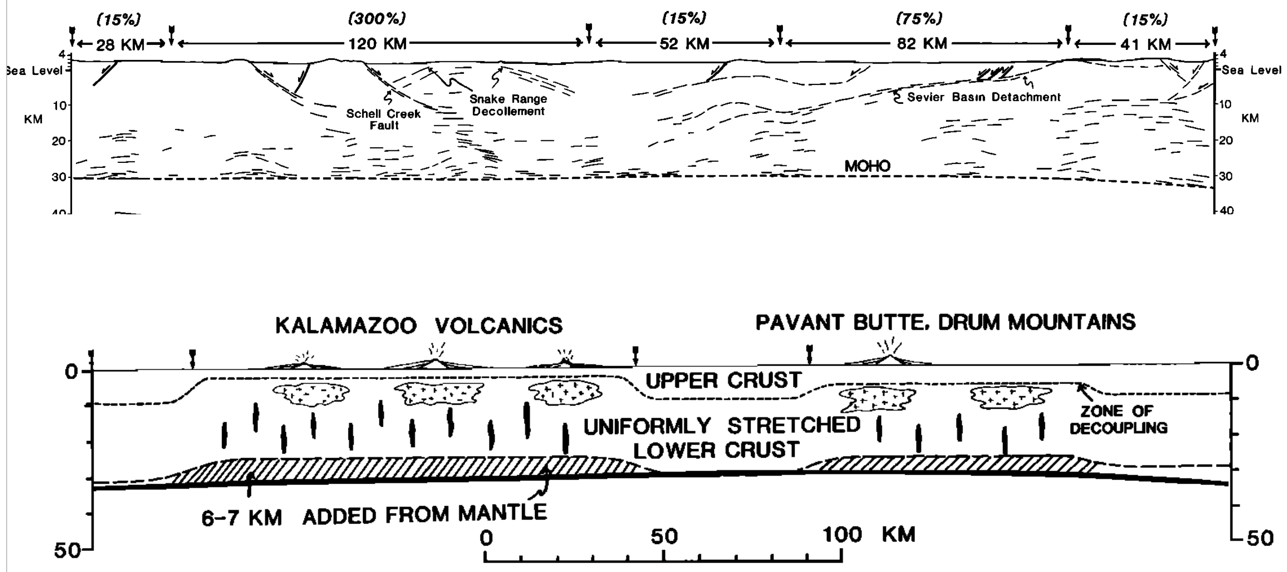


Fig. 3. A highly generalized present-day cross section of the eastern Great Basin that illustrates the two-layer, open-system model for crustal stretching. See text for discussion.

Gans, Tectonics, 1987

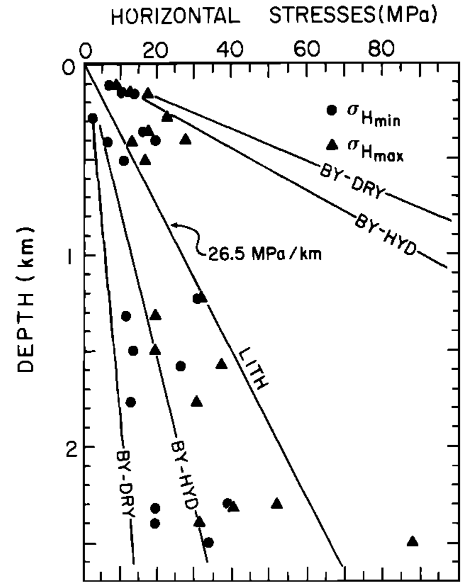


Fig. 1. Total horizontal stresses measured in southern Africa [*McGarr and Gay,* 1978]. The vertical total stress gradient (26.5 MPa/km) is shown along with Byerlee's law (BY) for hydrostatic pore pressure (HYD) and zero pore pressure (DRY).

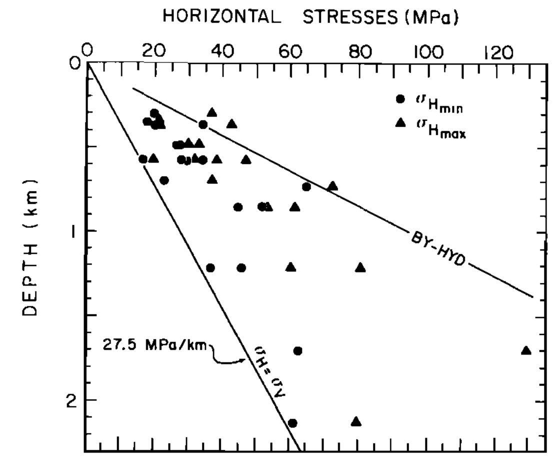


Fig. 3. Total horizontal stresses measured in Canada [*McGarr and Gay,* 1978]. Symbols as in Figure 1.

Brace & Kohlstedt,, JGR, 1980

$$\dot{\epsilon} = 7 \times 10^4 (\sigma_1 - \sigma_3)^3 \exp\left(\frac{-0.52\ \mathrm{MJ/mol}}{RT}\right) \qquad \sigma_1 - \sigma_3 < 200\ \mathrm{MPa}$$

$$\dot{\epsilon} = 5.7 \times 10^{11} \exp\left[\frac{-0.54\ \mathrm{MJ/mol}}{RT}\left(1 - \frac{\sigma_1 - \sigma_3}{8500}\right)^2\right] \qquad \sigma_1 - \sigma_3 > 200\ \mathrm{MPa} \tag{4}$$

where $\dot{\epsilon}$ is in $s^{-1}$ and $\sigma_1 - \sigma_3$ is in megapascals. The plastic deformation behavior of quartz appears to depend markedly on $OH^-$ content. We consider here experimental results on dry samples which should provide an upper limit to the strength of quartzite. Recent experiments of *Christie et al.* [1979] on dry quartzite at 800° and 900°C combined with the data of *Heard and Carter* [1968] yield the flow law

$$\dot{\epsilon} = 5 \times 10^6 (\sigma_1 - \sigma_3)^3 \exp\left(\frac{-0.19\ \mathrm{MJ/mol}}{RT}\right) \qquad \sigma_1 - \sigma_3 < 1000\ \mathrm{MPa} \tag{5}$$

where $\dot{\epsilon}$ is in $s^{-1}$ and $\sigma_1 - \sigma_3$ is in megapascals.

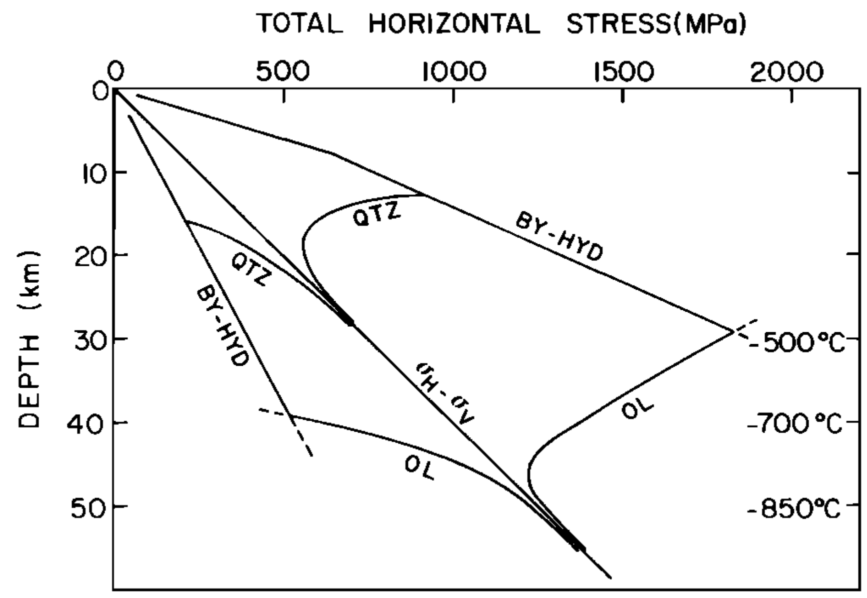


**Fig. 4.** Limiting values of total horizontal stress as a function of depth, based on Byerlee's law with hydrostatic pore pressure (BY-HYD) and the quartz (QTZ) and olivine (OL) flow laws adjusted to a strain rate of $10^{-15}\ s^{-1}$. The temperature profile $T(°K) = 350 + 15z(\mathrm{km})$.

Brace & Kohlstedt,, JGR, 1980

$$\dot{\epsilon} = 7 \times 10^4 (\sigma_1 - \sigma_3)^3 \exp\left(\frac{-0.52 \text{ MJ/mol}}{RT}\right)$$

$$\sigma_1 - \sigma_3 < 200 \text{ MPa}$$

(4)

$$\dot{\epsilon} = 5.7 \times 10^{11} \exp\left[\frac{-0.54 \text{ MJ/mol}}{RT}\left(1 - \frac{\sigma_1 - \sigma_3}{8500}\right)^2\right]$$

$$\sigma_1 - \sigma_3 > 200 \text{ MPa}$$

where $\dot{\epsilon}$ is in $s^{-1}$ and $\sigma_1 - \sigma_3$ is in megapascals. The plastic deformation behavior of quartz appears to depend markedly on $OH^-$ content. We consider here experimental results on dry samples which should provide an upper limit to the strength of quartzite. Recent experiments of *Christie et al.* [1979] on dry quartzite at 800° and 900°C combined with the data of *Heard and Carter* [1968] yield the flow law

$$\dot{\epsilon} = 5 \times 10^6 (\sigma_1 - \sigma_3)^3 \exp\left(\frac{-0.19 \text{ MJ/mol}}{RT}\right) \quad (5)$$

$$\sigma_1 - \sigma_3 < 1000 \text{ MPa}$$

where $\dot{\epsilon}$ is in $s^{-1}$ and $\sigma_1 - \sigma_3$ is in megapascals.

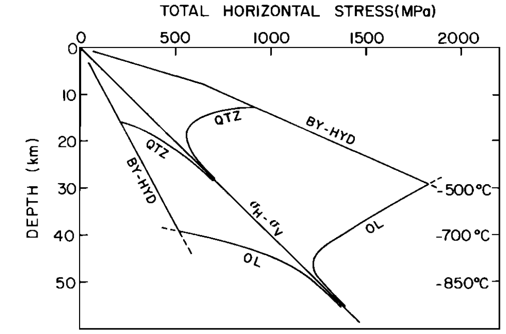


Fig. 4. Limiting values of total horizontal stress as a function of depth, based on Byerlee's law with hydrostatic pore pressure (BY-HYD) and the quartz (QTZ) and olivine (OL) flow laws adjusted to a strain rate of $10^{-15}$ $s^{-1}$. The temperature profile $T(°K) = 350 + 15z(km)$.

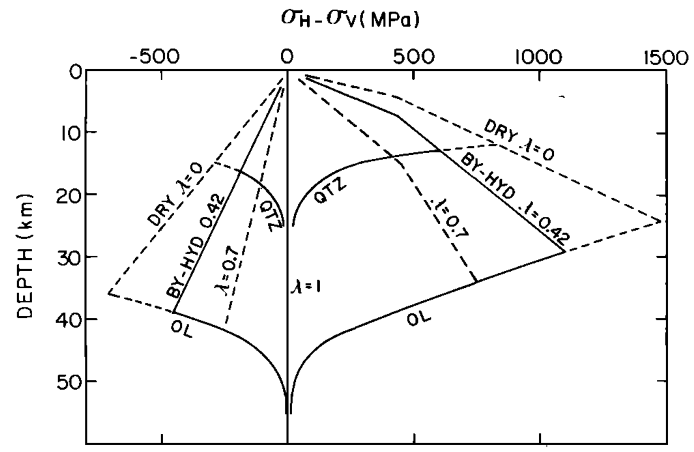


Brace & Kohlstedt,, JGR, 1980

Fig. 5. Difference between maximum or minimum horizontal stress and the vertical stress as a function of depth. Values of λ give pore pressure level. See also Figure 4.

## Compression, strain rate $10^{-15}$ $s^{-1}$, quartzite over olivene

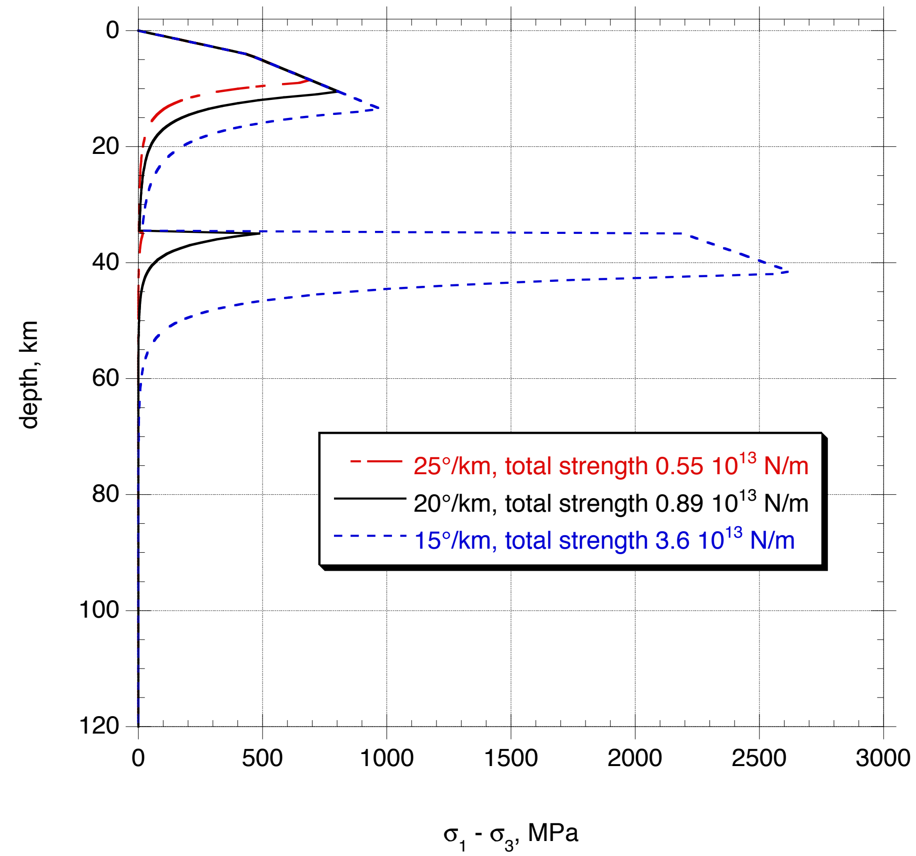

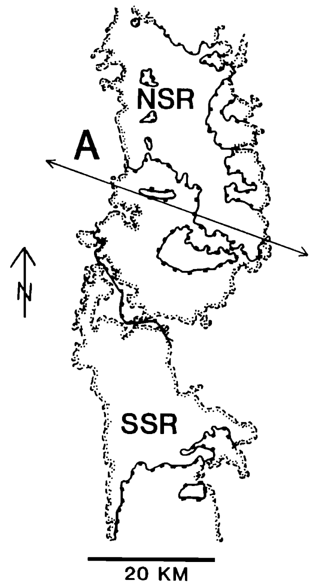


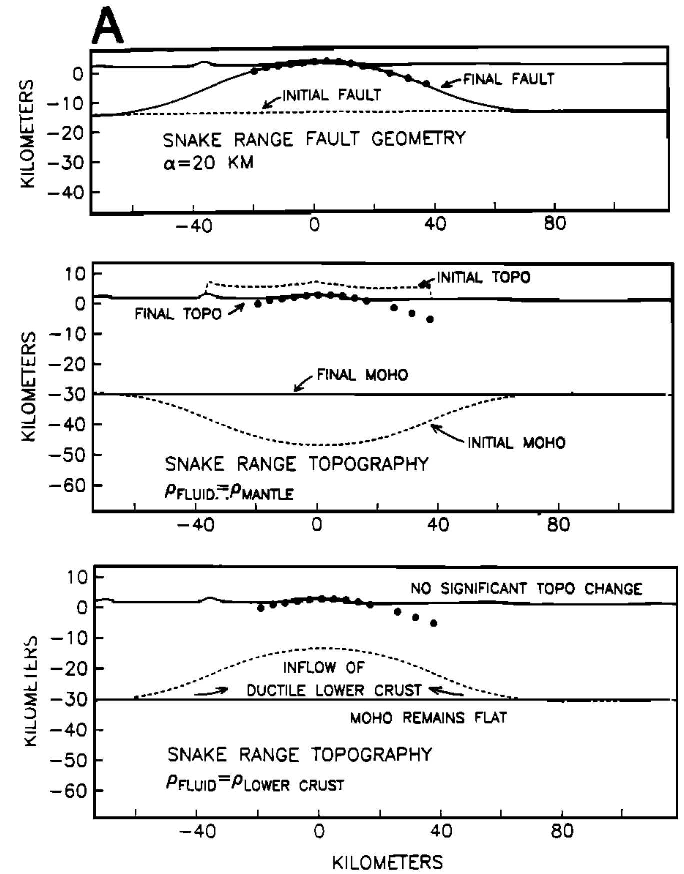


Fig. 3. Pre- and post-extensional fault geometry and topography for the Snake Range and Whipple Mountain detachment faults assuming that the fault was initially flat at a depth of 14 km (Figures 3a and 3c) or had an initial depth of 14 km at x=0 and dipped 20° E between the surface and 30 km depth (Figures 3b and 3d). Observed fault geometries (dots) and observed topography (solid lines) are shown in each panel (locations in Figure 2). Top panels in each Figure 3a-3d show the assumed initial (dashed line) and computed final (solid line) fault geometries.

Block and Royden, Tectonics, 1990

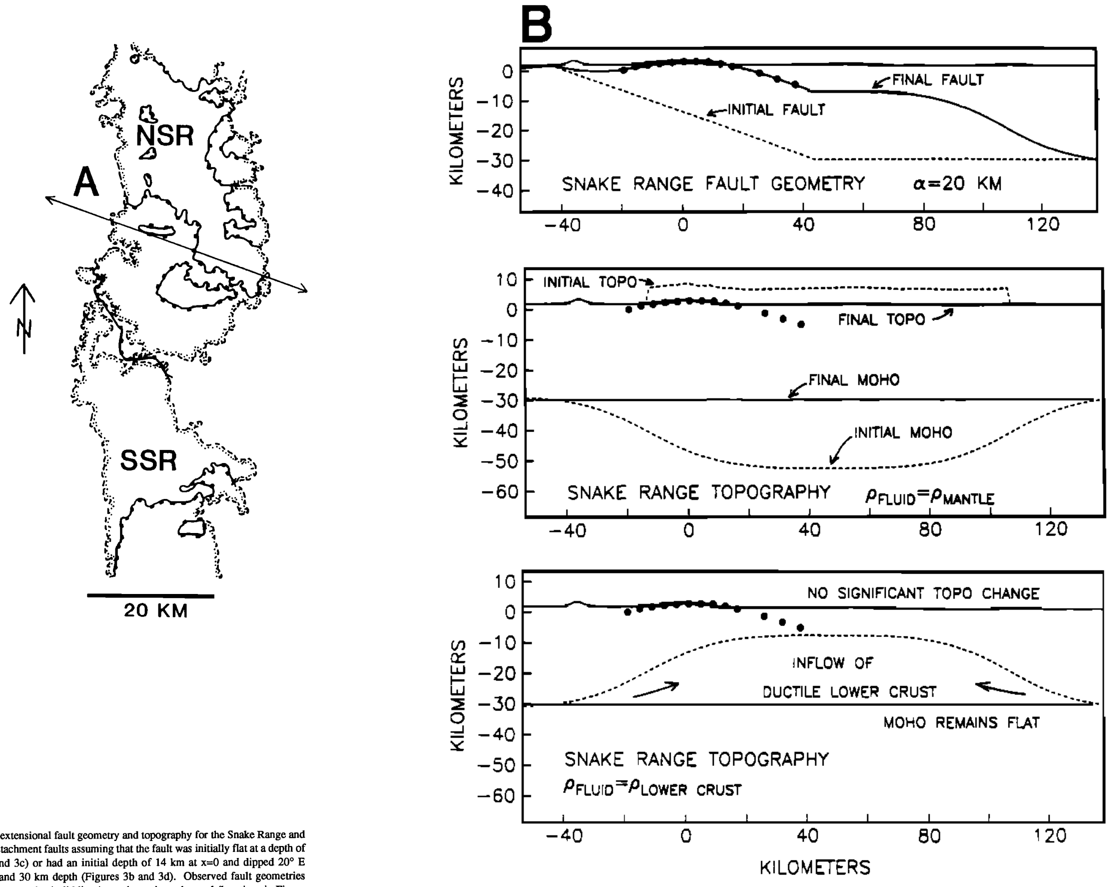


Fig. 3. Pre- and post-extensional fault geometry and topography for the Snake Range and Whipple Mountain detachment faults assuming that the fault was initially flat at a depth of 14 km (Figures 3a and 3c) or had an initial depth of 14 km at x=0 and dipped 20° E between the surface and 30 km depth (Figures 3b and 3d). Observed fault geometries (dots) and observed topography (solid lines) are shown in each panel (locations in Figure 2). Top panels in each Figure 3a-3d show the assumed initial (dashed line) and computed final (solid line) fault geometries.

Block and Royden, Tectonics, 1990

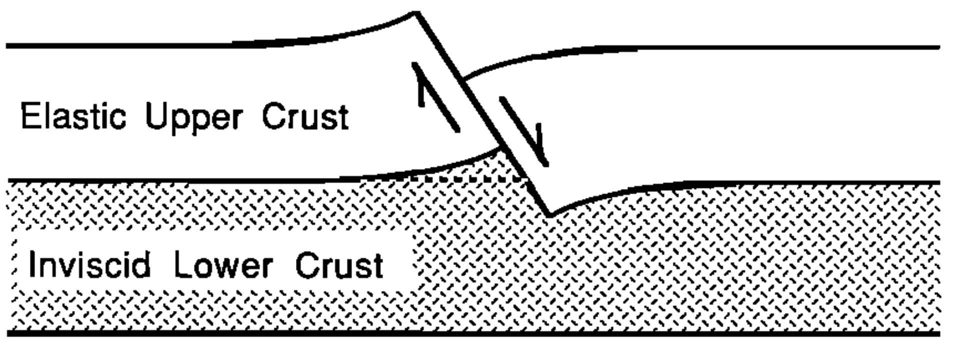


Fig. 4. Schematic of a normal fault cutting the entire upper crust. The base of the upper crust is always at a fixed depth, as shown by the dashed line.

Buck, Tectonics, 1988

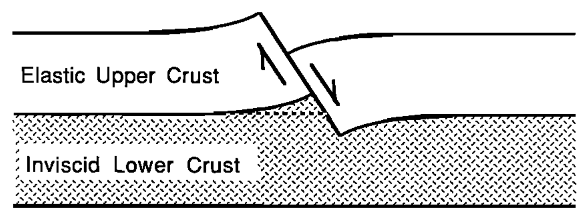


Fig. 4. Schematic of a normal fault cutting the entire upper crust. The base of the upper crust is always at a fixed depth, as shown by the dashed line.

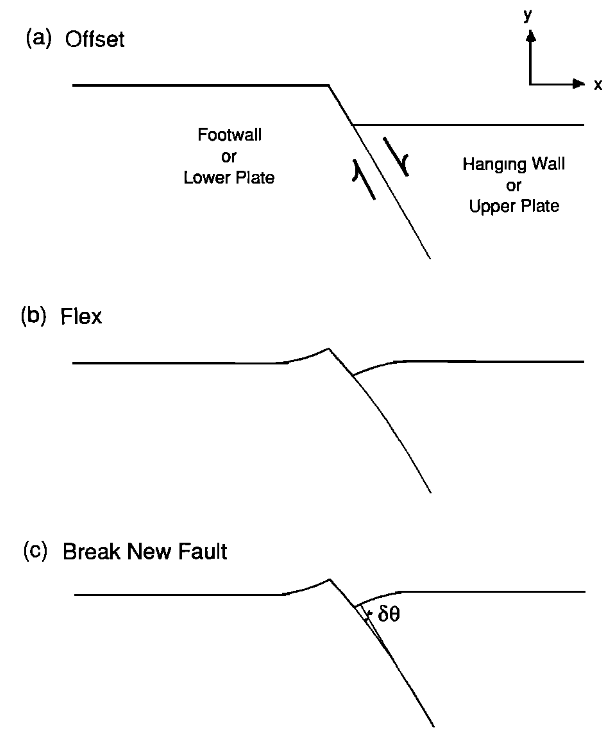


Fig. 6. Model formulation. (a) shows offset along a high-angle normal fault; (b) shows flexural response to the topographic load caused by the offset. The flexure causes rotation of the high angle normal fault over a flexural wavelength. In (c) the rotated fault is abandoned and a new extension of the fault, which is rooted in the lower crust, is cut through the top of the upper crust.

Buck, Tectonics, 1988

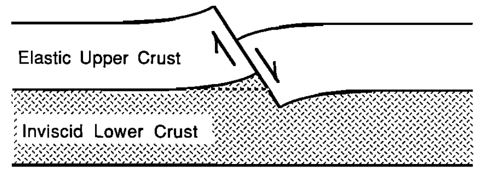


Fig. 4. Schematic of a normal fault cutting the entire upper crust. The base of the upper crust is always at a fixed depth, as shown by the dashed line.

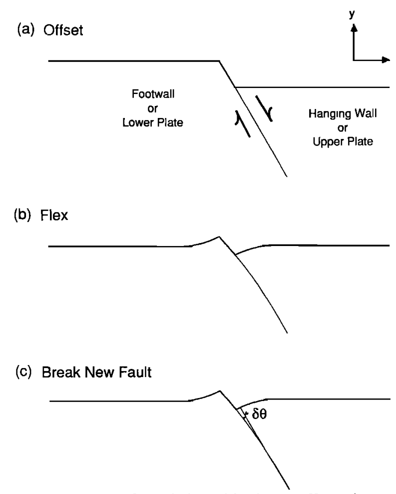


Fig. 6. Model formulation. (a) shows offset along a high-angle normal fault; (b) shows flexural response to the topographic load caused by the offset. The flexure causes rotation of the high angle normal fault over a flexural wavelength. In (c) the rotated fault is abandoned and a new extension of the fault, which is rooted in the lower crust, is cut through the top of the upper crust.

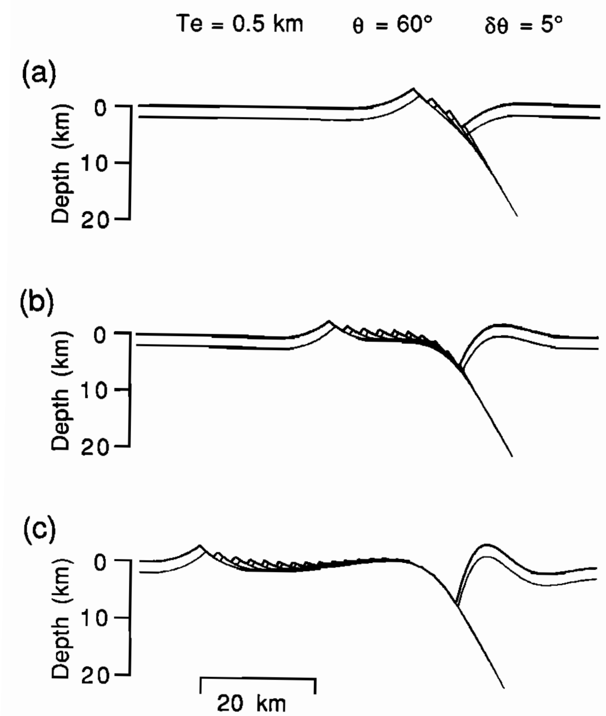


Fig. 7. Topography and positions of active and abandoned faults resulting from a calculation with a fault angle θ of 60°, an effective flexural rigidity of 0.5 km, and a rotation angle δθ of 5°. A line at 2 km depth is also plotted. Horizontal offsets of approximately (a) 15 km, (b) 30 km, and (c) 60 km are shown. There is no vertical exaggeration.

Buck, Tectonics, 1988

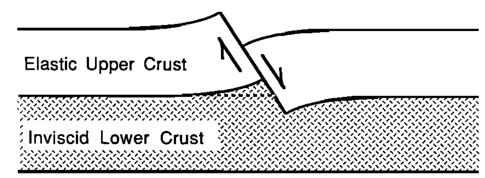


Fig. 4. Schematic of a normal fault cutting the entire upper crust. The base of the upper crust is always at a fixed depth, as shown by the dashed line.

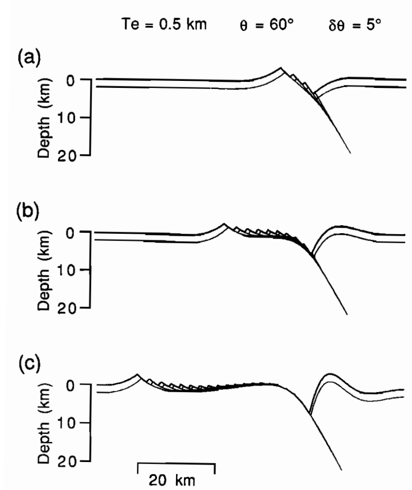


Fig. 7. Topography and positions of active and abandoned faults resulting from a calculation with a fault angle θ of 60°, an effective flexural rigidity of 0.5 km, and a rotation angle δθ of 5°. A line at 2 km depth is also plotted. Horizontal offsets of approximately (a) 15 km, (b) 30 km, and (c) 60 km are shown. There is no vertical exaggeration.

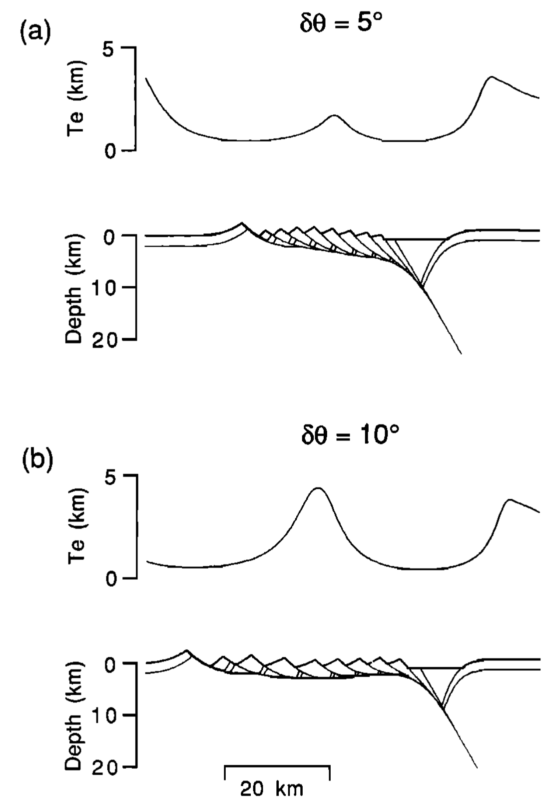


Fig. 12. Results of variable rigidity calculations in which sediment has been added to fill in all levels below 1000 m depth. Two cases of assumed angle of fault rotation before fault abandonment are shown: δθ = 5° and δθ = 10°.

Buck, Tectonics, 1988

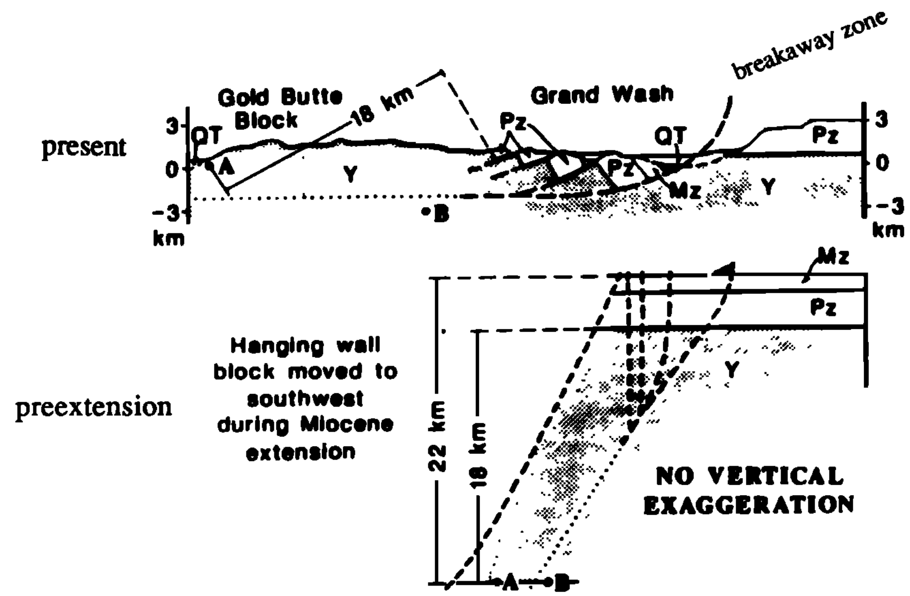


Fig. 2. Schematic cross section perpendicular to strike of transition zone at the latitude of Lake Mead showing inferred uplift of Gold Butte block. Location of profile shown in Figure 1. Modified from *Wernicke and Axen* [1988].

Kruse et al., JGR, 1991

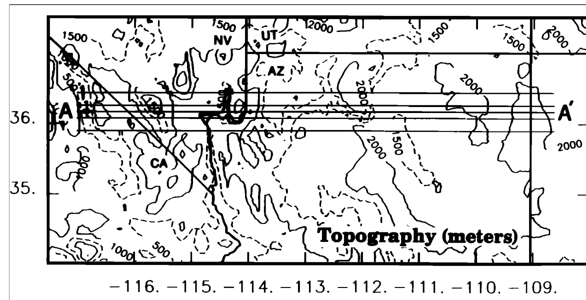


Fig. 3*a*. Topographic map of Lake Mead area and western Colorado Plateau. Thick lines mark state boundaries and the shore of Lake Mead. Thin straight lines show the location of topography profiles in Figure 4. Data taken from the NOAA TGP–0030 30' topography data set.

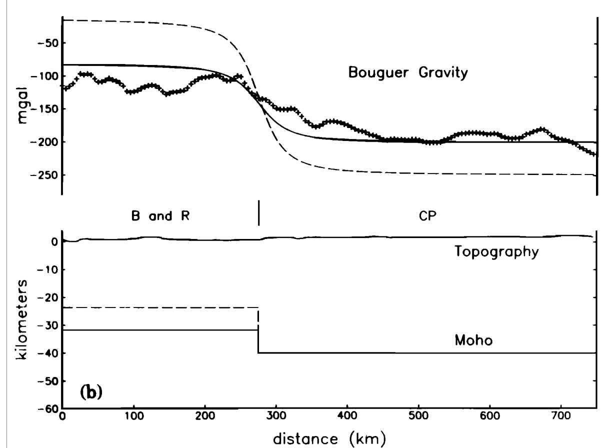


Fig. 5. (continued)

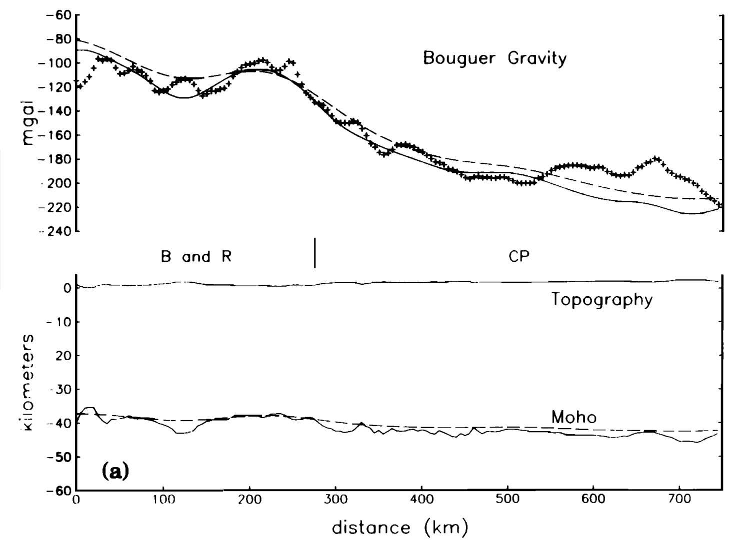


Fig. 5. Bouguer gravity anomalies predicted by simple compensation models. Topography data used in modeling are averaged from the five profiles of Figure 4. Crosses mark observed Bouguer gravity anomalies similarly averaged from the profiles of Figure 4. Short vertical line between upper and lower plots marks location of transition zone. (*a*) Solid curve shows local (Airy) compensation of topography by deflections of the Moho. Dashed curve shows compensation at Moho assuming a flexural rigidity of $10^{22}$ N m. (*b*) Bouguer gravity anomalies and Moho depths corresponding to uniform stretching of the lithosphere west of the transition zone according to the model of *McKenzie* [1978]. Solid curves indicate values associated with extension by a factor $\beta = 1.33$, resulting in 10 km of crustal thinning of crust initially 40 km thick. Dashed curves show values predicted from extension by a factor of 2 with 20 km of crustal thinning. Bouguer gravity anomalies are calculated assuming that the lithosphere in the extended region has thinned uniformly, maintaining a linear temperature gradient between the surface and a temperature of 1350°C at the base of the lithospheric plate. The unextended thickness of the lithospheric plate is set to 125 km. Deflections of the Moho maintain local (Airy) isostasy. To best fit the observed gravity data –200 mGal were added to the gravity predicted by the model for $\beta = 1.33$ (solid curves) and 250 mGal were added to the gravity predicted by the $\beta = 2$ (dashed curves) model.

Kruse et al., JGR, 1991

I think they assumed a Moho contrast of 600 kg m$^{-3}$

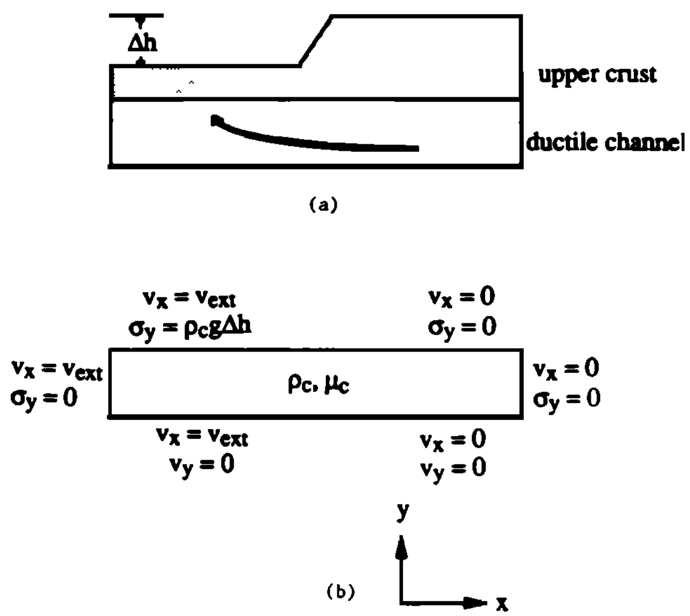


Fig. 7. *(a)* Schematic representation of ductile flow in response to uppe crustal thinning. *(b)* Boundary conditions on finite element models for ductile channel with a fixed lower boundary.

Kruse et al., JGR, 1991

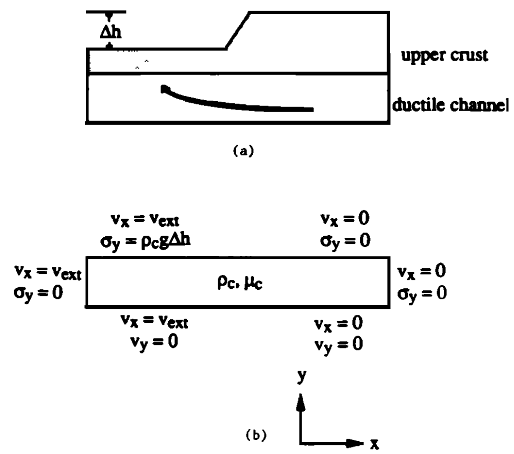


**Fig. 7.** *(a)* Schematic representation of ductile flow in response to upp crustal thinning. *(b)* Boundary conditions on finite element models for ductile channel with a fixed lower boundary.

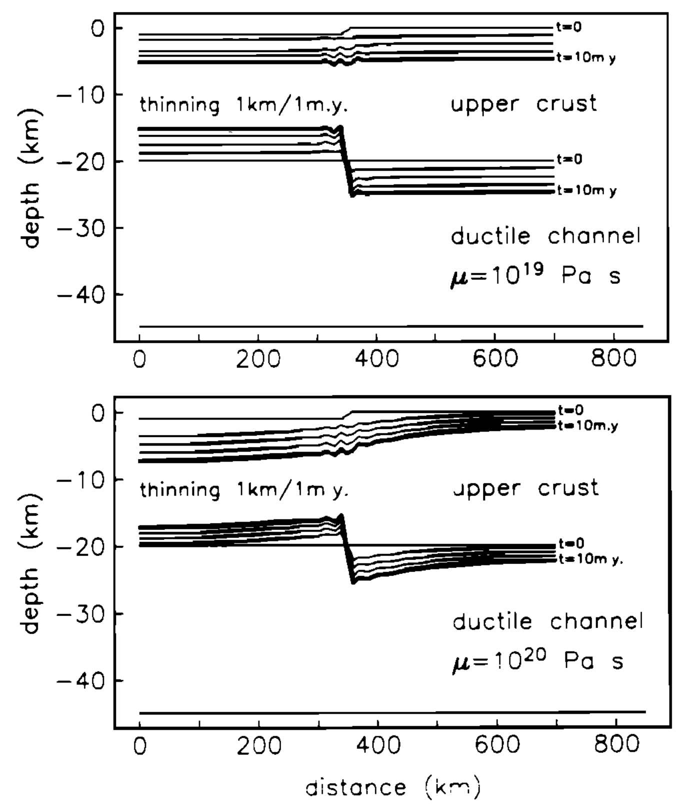


**Fig. 10.** Variations in total crustal thickness and ductile channel thickness for flow in a channel initially 25 km thick with a fixed lower boundary. The upper crust has zero flexural rigidity and thins over the left side of the mesh at a rate of 1 km/m.y.

Kruse et al., JGR, 1991

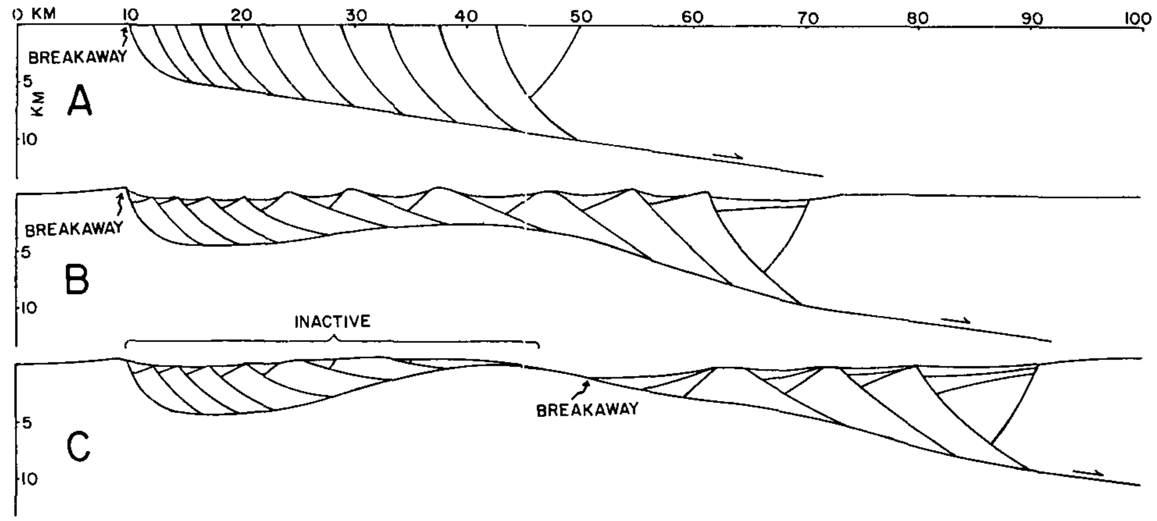


**Figure 2. Schematic diagram of warping and uplift of detachment fault. A: Inception of master detachment fault and subsidiary normal faults within upper plate. B: After 20 km of extension an antiformal warp has developed. Shape of warp and amount of uplift are depicted in listric model of Figure 1 (solid line). Antiform is becoming barrier to movement of upper plate from left, upper plate in area of synformal warping is becoming inactive, and one-sided denudation of antiform is about to begin. C: 20 km of one-sided denudation has resulted in further uplift and initial exposure of lower plate to subareal erosion. Shape of basal detachment fault and distribution of extension during one-sided denudation resemble planar detachment of Figure 1 and skewed distribution of extension (dashed line, Fig. 1), resulting in subdued arching of fault surface and amplified uplift in breakaway area.**

Spencer, Geology, 1984

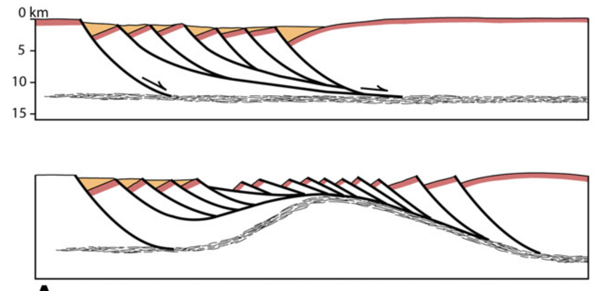


**A** Low-angle normal faults splay from a subhorizontal mylonitic shear zone

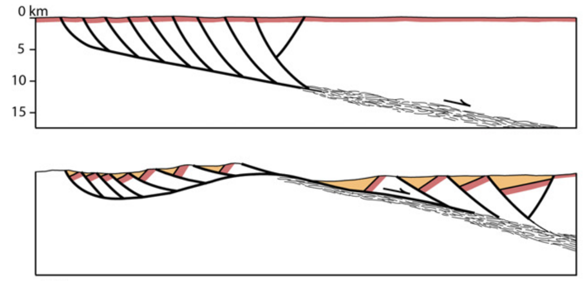


**B** Mylonitic shear zone and master detachment fault initiate at a shallow dip

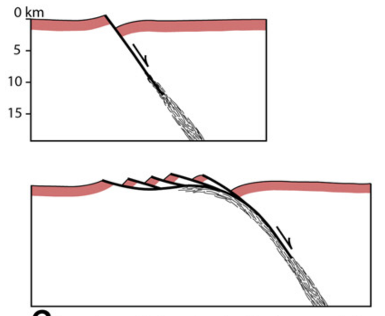


**C** Detachment fault and mylonitic shear zone initiate at a high angle and isostatically rotate to subhorizontal along a "rolling hinge"

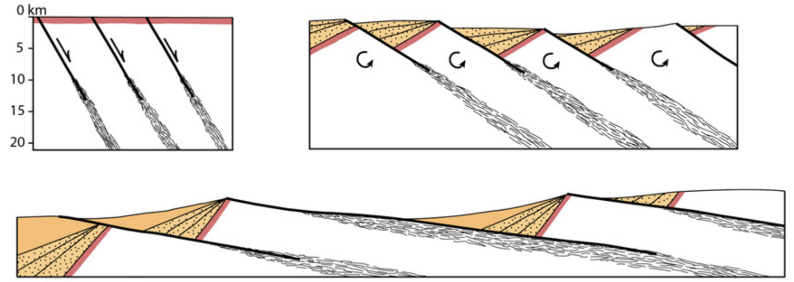


**D** Detachment faults and mylonitic shear zones initiate at moderate to steep angles (40-60°) and rotate to sub-horizontal via domino-style extension

Singleton & Mosher, J Struct Geol, 2012

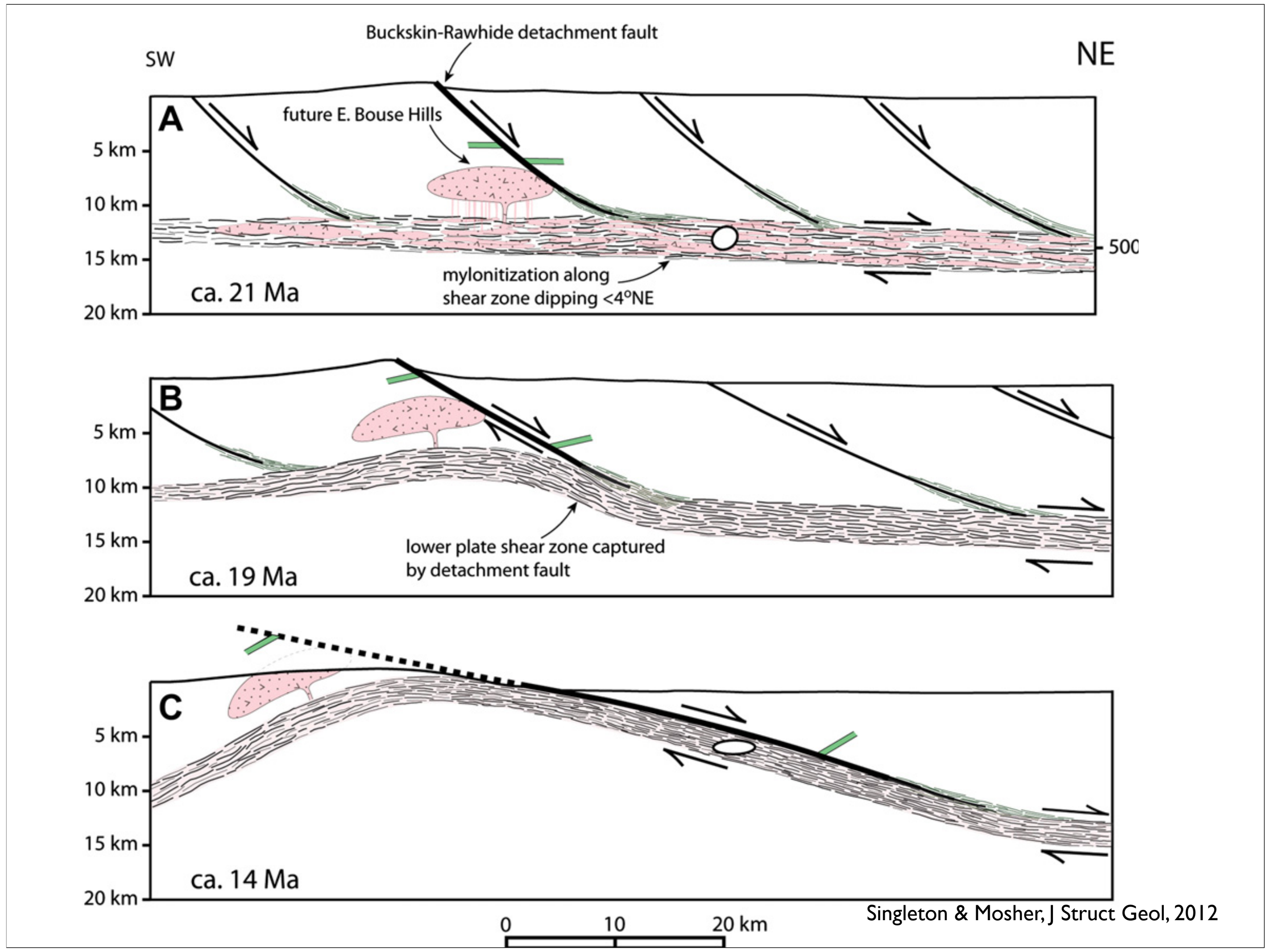


Based on temp est from quartz deformation in mylonites, argue shear zone initiated as a very flat feature but think that the upper plate faults were much steeper.